A new merged dataset for analyzing clouds, precipitation and atmospheric parameters based on ERA5 reanalysis data and the measurements of TRMM PR and VIRS

Lilu Sun[1], Yunfei Fu[1]

[1]School of Earth and Space Sciences, University of Science and Technology of China, Hefei, 230026, China

Correspondence to: Yunfei Fu (fyf@ustc.edu.cn)

Abstract. Clouds and precipitation have vital roles in the global hydrological cycle and the radiation budget of the atmosphere–Earth system and are closely related to both the regional and global climate. Changes in the status of the atmosphere inside clouds and precipitation systems are also important, but the use of multi-source datasets is hampered by their different spatial and temporal resolutions. We merged the precipitation parameters measured by the Tropical Rainfall Measuring Mission (TRMM) Precipitation Radar (PR) with the multi-channel cloud-top radiance measured by the Visible and Infrared Scanner (VIRS) and atmospheric parameters in the ERA5 reanalysis dataset. The merging of pixels between the precipitation parameters and multi-channel cloud-top radiance was shown to be reasonable. The 1B01-2A25 dataset of pixel-merged data (1B01-2A25-PMD) contains cloud parameters for each PR pixel. The 1B01-2A25 gridded dataset (1B01-2A25-GD) was merged spatially with the ERA5 reanalysis data. The statistical results indicate that gridding has no unacceptable influence on the parameters in the 1B01-2A25-PMD. In one orbit, the difference in the mean value of the near-surface rain rate and the signals measured by the VIRS was no more than 0.87 and the standard deviation was no more than 2.38. The 1B01-2A25-GD and ERA5 datasets were spatiotemporally collocated to establish the merged 1B01-2A25 gridded dataset (M-1B01-2A25-GD). Three case studies of typical cloud and precipitation events were analyzed to illustrate the practical use of the M-1B01-2A25-GD. This new merged gridded dataset can be used to study clouds and precipitation systems and provides a perfect opportunity for multi-source data analysis and model simulations. The data which were used in this paper are freely available at http://doi.org/10.5281/zenodo.4458868 (Sun and Fu, 2021).

1   Introduction

28 Clouds and precipitation are the result of interactions among several different atmospheric parameters.

29 They have a crucial role in global hydrological and energy cycles which can be used to represent changes

30 in the Earth's weather and climate (Hartmann and Short, 1980; Liou, 1986; Wetherald and Manabe, 1988;

31 Baker, 1997; Houze, 1997; Roscow et al., 1999; Oki and Kanae, 2006; Lau and Wu, 2010; Fu and Zhang,

32 2018). More than two-thirds of all precipitation falls in the tropics and subtropics. The atmosphere

33 obtains energy from the release of the latent heat of condensation during precipitation and this is one of

34 the main drivers of atmospheric circulation at low latitudes. Precipitating clouds also influence the

35 Earth's radiation budget (Fu et al., 2006; Sassen et al., 2009; Kienast-Sjögren et al., 2016; Fu and Zhang,

36 2018; Gao et al., 2018). Atmospheric parameters (e.g., the temperature, pressure and wind fields) can be

37 used to demonstrate changes in atmospheric status and the development of cloud and precipitation

38 systems (Wang et al., 2015; Zheng et al., 2015; Pan and Fu, 2015; Xia and Fu, 2016; Wang et al., 2017).

39 Analysis of the complex distribution of clouds and precipitation, especially their 3D structures, helps to

40 require a detailed understanding of the microphysical processes and thermodynamic structure of clouds.

41 The horizontal structure represents the extent of the system, whereas the thermodynamic structure and

42 microphysical processes inside clouds during the phase transition of water can be represented by the

43 vertical structure (Houze, 1981; Szoke et al., 1986; Hobbs, 1991; Zipser and Lutz, 1994; Yuter and Houze,

44 1995; Liu and Fu, 2001; Luo et al., 2009). A comprehensive understanding of the 3D structure of

45 precipitation and clouds will improve precipitation retrieval algorithms and model simulations (Wilheit

46 et al., 1977; Petty, 1994; Kummerow et al., 1996; Olson et al., 1996; Iguchi et al., 2000; Tustison et al.,

47 2002; Min et al., 2013).

48 Satellite remote sensing technology has developed rapidly in recent years. The first space-borne active

49 radar is the Precipitation Radar (PR) onboard the Tropical Rainfall Measurement Mission (TRMM)

50 (Kummerow et al., 1998; Kummerow et al., 2000; Kozu et al., 2001). The main aim of the TRMM is the

51 effective observation of precipitation and energy exchange in tropical and subtropical regions. The

52 unique instruments onboard the satellite provide an excellent opportunity to study the 3D structure of

53 precipitation (Nesbitt et al., 1999; Schumacher and Houze, 2003; Durden et al., 2003; Li and Fu, 2005;

54 Liu and Zipser, 2009), whereas the Visible and Infrared Scanner (VIRS) provides characteristics of cloud

55 parameters near the cloud-top (Liu and Fu, 2010; Fu, 2014; Yang et al., 2014; Chen and Fu, 2017).

56 Many studies of the 3D structure of clouds and precipitation have been based on TRMM measurements

57   (Fu and Liu, 2001; Lu et al., 2016; Wang and Fu, 2017; Luo et al., 2020). Chen and Fu (2015) focused

58   on the characteristics of precipitation and thermal infrared signals of clouds in typhoon and non-typhoon

59   precipitation in eastern Asia by analyzing merged data between the PR and the VIRS pixels. Results

60   showed that the most intense typhoon precipitation occured on the ocean surface in eastern Asia. Non-

61   typhoon precipitation was the main type of precipitation in the rainy season, but typhoon precipitation

62   made the largest contributed to the total amount of precipitation. Yang et al. (2014) statistically analyzed

63   10-year data from the TRMM PR and VIRS and found that the cloud height and thickness of anvil clouds

64   over land were always greater than those over the sea surface, and anvil clouds had a greater optical

65   thickness over the land surface and more small ice particles.

66   Liu and Fu (2001) classified tropical precipitation into two main types (deep convective and stratiform)

67   using the main component method. The mean rain rate profiles of deep convective rain had four layers,

68   whereas stratiform precipitation had only three. Differences in the slopes of the mean profiles can be

69   used to illustrate the microphysical processes at different vertical structure of the rainfall. Liu and Fu

70   (2007) compared rain rate profiles from the Tibetan Plateau, eastern Asia and the tropics. It was found

71   that there was little stratiform precipitation on the Tibetan Plateau, but deep weak convective

72   precipitation was frequently detected in this region. The slope of the mean deep weak convective profile

73   was greater than that for convective precipitation, which meant that more latent heat was released to heat

74   the middle and upper atmosphere. Fu et al. (2008) found that the tops of precipitating clouds were about

75   4–6 km higher than that in the surrounding area. The difference in the clouds tops height led to a tower-

76   like structure over the Tibetan Plateau, which can heat the upper troposphere more easily.

77   Recent researchs has investigated the status of the atmosphere in clouds and precipitation systems (Wang

78   and Fu, 2017; Li et al., 2018). In addition to observations from surface meteorological stations,

79   atmospheric parameters can be obtained from sounding balloons, sensors onboard planes and model

80   simulations. Because of the uneven distribution of ground meteorological stations, the unpredictable

81   routes of sounding balloons and the limited detection area of planes. We therefore analyzed the

82   characteristics and distribution of atmospheric parameters inside clouds and precipitation systems using

83   the ERA5 reanalysis dataset.

84   It is impossible to obtain simultaneous and comprehensive information using a single detection method

85   or dataset as a result of the different ways of obtaining the cloud, precipitation and atmospheric

parameters. The optimum choice to overcome this problem is to combine multiple remote sensing measurements and multi-source datasets (Fu et al., 2013; Chen and Fu, 2017). Hawkins et al. (2008) combined multiple source datasets, including satellite cloud imagery captured by cloud profile radar and stationary satellites, observations from experimental planes and model simulations. Fu et al. (2013) used moving surface fitting method to combine TRMM TMI and PR pixel data. The differences in the mean, standard deviation and frequency distribution between the original and merged data are analyzed to validate the accuracy. Wang et al. (2017) merged the TRMM PR 2A25 products with the IGRA dataset to investigate the profiles of temperature and humidity for the convective and stratiform precipitation. The merged data can be used to determine the vertical structure of precipitating clouds and the atmospheric parameters in typhoon, frontal and thermal convective precipitation systems.

VIRS pixels can be merged onto PR pixels in a similar way to verify precipitating clouds. The results of this type of merger have shown that the reflectivity in the visible channel near the precipitating cloud-top is bigger than 0.5 in the intertropical convergence zone, convergence zone of the southern hemisphere, the monsoon region of Asia, the tropical regions of Africa, North America and South America. The reflectivity on land is greater than that on the sea surface (Fu et al., 2011). Liu and Fu (2010) verified precipitating clouds from several typhoon and frontal precipitation events in eastern China based on the same merged dataset. Precipitating clouds cannot be classified precisely by relying on only the thermal infrared brightness temperature and other parameters are needed to improve the accuracy, such as the ratio between the signals in the visible and near infrared channels.

The various temporal and spatial resolutions of different datasets can cause problems and it is better to merge data from multiple instruments onboard the same satellite, such as the TRMM. The ERA5 reanalysis dataset has a suitable temporospatial resolution for merging with the TRMM data to supplement the atmospheric parameters. This new merged dataset includes comprehensive parameters that can be used to analyze the features of the precipitation and clouds systems.

We merged TRMM PR and VIRS measurements with the ERA5 reanalysis data at the same spatiotemporal resolution to establish a new dataset of precipitation, cloud and atmospheric parameters. Section 2 describes the data and merging methods. Section 3 presents the main results about the influence of the merger on the original data during the merging process and the pratical applications of the new merged dataset. Section 4 discusses the advantages of the dataset and future work in the progress. Access

115 to the dataset is introduced in Section 5 and conclusions are presented in Section 6.

2 Data and methods

2.1 Tropical Rainfall Measurement Mission

The TRMM was launched in November 1997 as a joint mission between the US National Aeronautics and Space Administration (NASA) and the Japan Aerospace Exploration Agency (JAXA). The objectives of the TRMM are to obtain satellite measuremenets of rainfall and energy exchange in tropical and subtropical regions (https://trmm.gsfc.nasa.gov/overview_dir/background.html). The TRMM is a non-solar synchronous polar orbiting satellite in a 350 km (402 km after an orbital boost on 7 August 2001) circular orbit with an inclination angle of 35°. The TRMM observes a specific location between 38° S and 38° N every 45 days. One complete scan of the orbit takes about 96 minutes, so there are 16 orbits in one day (Simpson et al., 1996; Kummerow et al., 1998).

2.2 PR and 2A25 dataset

The PR was the first space-borne precipitation radar onboard the TRMM. It is a 128-element active phased array system operating at 13.8 GHz (Kozu et al., 2001). The PR antenna scans in the cross-track direction over 17° in a 215 km (220 km after the orbital boost) swath width. There are 49 pixels in each scan line. The PR measures the spatial distribution of the intensity of precipitation from mean sea-level to 20 km (80 layers in total) and has a horizontal resolution of 4.5 km at nadir (5 km after the orbital boost). The vertical resolution of the PR is 0.25 km.

The 2A25 data produced by NASA Goddard Space Flight Center is the second-level data product of the TRMM PR. The dataset includes the scan time, geolocation information, rain type, 3D rain rate and so on. The TRMM PR algorithm classifies the type of rain into convective, stratiform and "other" (Awaka et al., 1997; Hayasaka et al., 1998).

2.3 VIRS and 1B01 datasets

The VIRS antenna scans in the cross-track direction over 45° in a 720 km (833 km after the orbital boost) swath width. There are 261 pixels in each scan line and the horizontal resolution is 2.2 km at nadir (2.4 km after the orbital boost). The VIRS receives upward radiation at five wavelengths ranging from the visible to the far infrared: 0.63 µm (CH1), 1.6 µm (CH2), 3.7 µm (CH3), 10.8 µm (CH4) and 12.0 µm

142 (CH5).

143 The 1B01 dataset is the first-level data product of the VIRS. The 1B01 data include the reflectivity in

144 CH1 and CH2 (RF1 and RF2) and the infrared radiation brightness temperature ($TB_{3.7}$, $TB_{10.8}$ and $TB_{12.0}$)

145 in CH3, CH4 and CH5, which are calibrated from the spectral signals measures by the VIRS.

2.4 ERA5 reanalysis dataset

147 The ERA5 renalysis dataset is the fifth (latest) generation of global atmospheric reanalysis datasets

148 produced by the European Centre for Medium-Range Weather Forecasts. The ERA5 dataset is based on

149 the Integrated Forecasting System Cy41r2 model and assimilates more model simulation outputs and

150 observational results. The ERA5 dataset is superior to previous versions in terms of its hourly output,

151 finer spatial resolution (0.25°) and abundant parameters (Zhao et al., 2019; Hersbach et al., 2020). We

152 used the hourly atmospheric parameters (divergence, geopotential height, specific humidity, wind field,

153 vertical velocity and temperature) on pressure levels for 32 layers from 1000 to 10 hPa. All the pressure

154 layers are used during the data merging, except the uppermost pressure layers from 1 to 7 hPa, which are

155 rarely used in studies.

2.5 2A25 and 1B01 merged data

157 The characteristics of precipitation and clouds are shown by identifying precipitating clouds from the

158 PR and detecting radiance near the top of the cloud by the VIRS (Liu and Fu, 2010; Fu et al., 2011;

159 Chen et al., 2018). The 2A25 and 1B01 data products (derived from the TRMM PR and VIRS,

160 respectively) can be collocated to establish a merged dataset to provide comprehensive information

161 about precipitation and clouds systems. The feasibility of data merging depends largely on the sensor

162 settings, such as the temporal sampling rate, the synchronism of detection and the spatial resolution.

163 The PR and the VIRS are both the main sensors onboard the TRMM. Despite the difference in spatial

164 resolution between 1B01 and 2A25, the time lag between detections of the same target is less than 1

165 minute. The similar cross-track scanning modes make it reasonable to consider that the PR and VIRS

166 are roughly synchronous in their detection area. It is therefore feasible to combine these two orbit-level

167 data products. Spatial merging is the only process that needs to be taken into account because of the

168 quasi-synchronicity between the TRMM PR and VIRS.

169 On account of the diverse orbital swath widths and spatial resolutions, the horizontal resolution of the

170   1B01 is decreased to match that of the 2A25 so that data merging can be easily achieved. The VIRS

171   pixels are merged onto the PR pixels through a weight-averaged method. The spectral signals are

172   calculated near the PR pixel and there are usually about seven VIRS pixels near one PR pixel (Fu et al.,

173   2011). The primary data of the 1B01 include the reflectivity at CH1 and CH2 (RF1 and RF2), the

174   equivalent brightness temperature of a black body at CH3, CH4 and CH5 ($TB_{3.7}$, $TB_{10.8}$ and $TB_{12.0}$), the

175   instantaneous near-surface rain rate and the vertical structure of precipitation in 2A25. All the VIRS

176   signals are within the resolution of the PR pixel which can be used to study the characteristics of

177   precipitating clouds. The 1B01-2A25 pixel-merged data (1B01-2A25-PMD) are then established. The

178   spatial resolution of 1B01-2A25-PMD is 5 km and the swath width is 220 km (Liu and Fu, 2010;

179   Chen and Fu, 2015; Chen and Fu, 2017).

180   **2.6   Gridding of the 1B01-2A25-PMD**

181   Because the 1B01-2A25-PMD contains orbit-level data, data gridding is necessary to merge these data

182   with the ERA5 data. The 1B01-2A25-PMD is gridded between 40° S and 40° N and the spatial

183   resolution is 0.25°, in agreement with the resolution of the ERA5 data. Taking the near-surface rain rate

184   as an example, we first sum the near-surface rain rate of the pixels in the same grid and then counting

185   the number of precipitating pixels in one grid and dividing the total rain rate by the total number of

186   precipitating pixels to obtain the near-surface rain rate of one grid. The grid-level dataset, namely, the

187   1B01-2A25 gridded data (1B01-2A25-GD) is calculated in the same way. The dataset includes the

188   gridded spectral signals measured by the VIRS in each PR pixel. The precipitation is classified into

189   three types: total precipitation, convective precipitation, and stratiform precipitation. The PR is a Ku-

190   band radar with a working frequency of 13.8 GHz and a wavelength of 2.2 cm. The sensitivity of the

191   PR is 16 dBZ and the minimum rain rate it can detect is about 0.4 mm h^{-1}. Only pixels with a near-

192   surface rain rate greater than 0.4 mm h^{-1} are calculated.

193   **2.7   Merging the ERA5 and 1B01-2A25-GD**

194   We merged the ERA5 data onto the 1B01-2A25-GD grid to explore the atmospheric status of the

195   precipitation and clouds systems measured by the sensors onboard the TRMM. The ERA5 dataset has

196   hourly outputs and the ERA5 parameters were therefore interpolated according to the grid times in the

197   1B01-2A25-GD. The geolocation of the ERA5 grid was selected to match that of the 1B01-2A25-GD.

198   The merged 1B01-2A25 gridded dataset (M-1B01-2A25-GD) was therefore obtained, which includes

199   geolocation information, the time of the grid and parameters for precipitation, clouds and the

200   atmospheric status. Table 1 contains critical informations of the M-1B01-2A25-GD.

201   **Table 1. Critical informations of the M-1B01-2A25-GD**

M-1B01-2A25-GD	
Spatial resolution	0.25°
Temporal resolution	Hourly
Main parameters	profiles of rain rate and precipitation reflectivity factor, near-surface rain rate, rain type, spectral signals measured by the VIRS, temperature, specific humidity, wind field, geopotential height, divergence and vertical velocity
Swath width	220 km
Vertical coverage	0 to 20 km (precipitation profile)
	1000 hPa to 10 hPa (atmospheric parameters)
Vertical resolution	0.25 km (precipitation profile)
	32 pressure layers (atmospheric parameters)

202   **3   Results**

203   **3.1   Evaluation of the 1B01-2A25-PMD**

204   The horizontal resolution of the 1B01 is decreased in the 1B01-2A25-PMD as a result of merging onto

205   the PR pixels. The detection field of the merged data is narrower than that in the 1B01 and is about the

206   same as the swath width of the PR. The influence on the original data in 1B01 after merging is

207   presented based on comparisons between the probability distribution functions (PDFs). Taking an

208   arbitrary orbit for example, orbit 37362 on 5 June 2004. Comparisons are made between the signals in

209   five spectral channels in the 1B01 and 1B01-2A25-PMD. Figure 1a–e represent the PDFs of RF1, RF2,

210    $TB_{3.7}$, $TB_{10.8}$ and $TB_{12.0}$ in the 1B01 and 1B01-2A25-PMD, respectively.
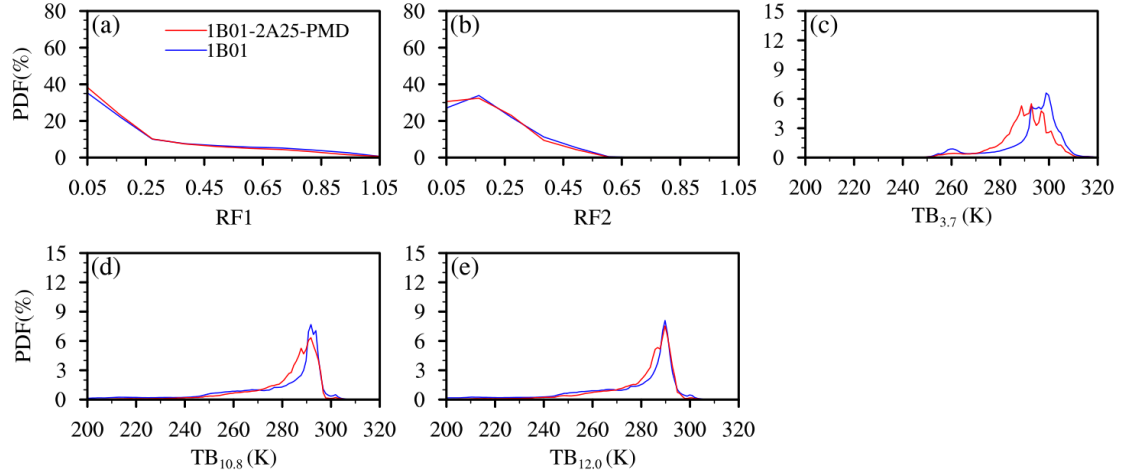
Figure 1: PDFs of (a) RF1, (b) RF2, (c) $TB_{3.7}$, (d) $TB_{10.8}$ and (e) $TB_{12.0}$ in the 1B01 (blue line) and 1B01-2A25-PMD (red line) in orbit number 37362 on 5 June 2004.

Figure 1a and 1b show that there is no clear change in RF1 and RF2 after merging. The shape of the PDFs are nearly the same in the 1B01-2A25-PMD and 1B01, with the reflectivity ranging from 0.05 to 1.05, but concentrate in the range 0.05–0.3. By contrast, there is a clear variation in $TB_{3.7}$ after merging (Fig. 1c). The PDF of the 1B01 is a single peak with a maximum at 300 K and a sub-peak at 290 K. The PDF of the 1B01-2A25-PMD shows a multi-peak shape, with the peaks mostly in range 280–300 K. $TB_{3.7}$ ranges from 250 to 320 K in both the 1B01 and 1B01-2A25-PMD. The difference in $TB_{3.7}$ between the 1B01 and 1B01-2A25-PMD is probably caused by the uneven cloud distribution. Also the difference in $TB_{10.8}$ signal is noticeable. Although the ranges and the maximum of the $TB_{10.8}$ nearly unchanged after merging, but the shape of the PDF line is different near the maximum. $TB_{12.0}$ have the same distribution after merging. The signals vary from 240 to 300 K and the maxima of the PDFs are both at about 290 K. Although the PDFs of the original and merged datasets are similar, there are slight differences in the peak values. The PDFs of the 1B01-2A25-PMD show lower peaks as a result of data averaging inside the grid (Fig. 1c and 1d).

Two regions are selected to analyze the distinctive changes in $TB_{3.7}$ after merging onto the PR pixels: (1) a region that mainly contains cloudy pixels (the cloudy region), and (2) a region that mainly contains clear sky pixels (the clear sky region). When the radiance brightness temperature is greater than 290 K, the pixel is classified as a clear sky pixel, whereas cloudy pixels are classified as those pixels in which the near-surface rain rate is greater than 0.4 mm h^{-1}.
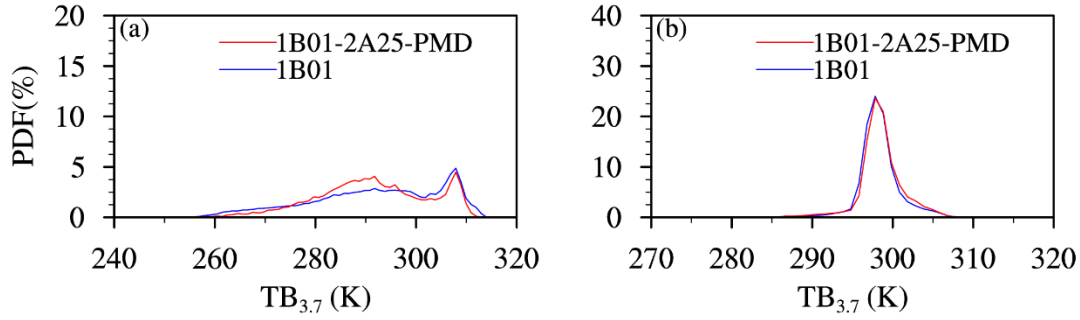
Figure 2: PDFs of TB₃.₇ in (a) cloudy regions and (b) clear sky regions in the 1B01 (blue line) and 1B01-2A25-PMD (red line) in orbit number 37362 on 5 June 2004.

Fig. 2 shows the PDFs of TB$_{3.7}$ in these two regions. TB$_{3.7}$ ranges from 260 to 315 K in the cloudy region and the maximum value (310 K) is almost the same in both the 1B01 and 1B01-2A25-PMD datasets (Fig. 2a). This similarity is also seen in the PDF of TB$_{3.7}$ in the clear sky region, where TB$_{3.7}$ varies between 290 and 310 K with a single-peak structure and a maximum at 300 K (Fig. 2b). In a word, the merging process between the PR and the VIRS pixels is considered lead to no dramatic variations on the original data.

3.2 Evaluation of the 1B01-2A25-GD

The 1B01-2A25-PMD was gridded to match the ERA5 reanalysis data spatially and this dataset is referred to as the 1B01-2A25-Gridded Data (1B01-2A25-GD). Data processing studies have shown that the precision of the spatial resolution of a dataset can affect the accuracy and physical characteristics of the data (Heng and Fu, 2014) and therefore it is essential to evaluate the effects of the gridding process. As an example, Figure 3 compares the near-surface rain rate and the CH1–CH5 signals of the original and gridded data for orbit 37362 on 5 June 2004 in both the 1B01-2A25-PMD and 1B01-2A25-GD.
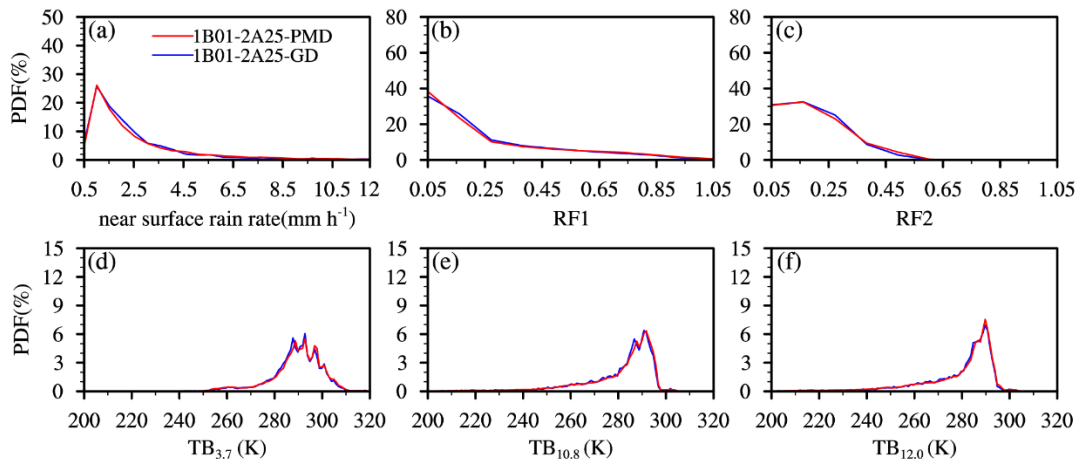
Figure 3: PDFs of (a) the near-surface rain rate, (b) RF1, (c) RF2, (d) TB₃.₇, (e) TB₁₀.₈ and (f) TB₁₂.₀ in the

250 **1B01-2A25-PMD (red line) and 1B01-2A25-GD (blue line) in orbit number 37362 on 5 June 2004.**

251 Figure 3a shows that the PDF of the near-surface rain rate in the 1B01-2A25-PMD has a single peak and

252 the rain rate mainly ranges from 1 to 3 mm h^{-1}. The PDF of the gridded data is nearly the same as that

253 of the original data, so gridding has little influence on the near-surface rain rate. The PDFs for RF1 and

254 RF2 are also largely unchanged. RF1 varies from 0.05 to 1.05 and RF2 is mainly in the range 0.05–0.55

255 (Fig. 3b, 3c). The brightness temperature ($TB_{3.7}$, $TB_{10.8}$ and $TB_{12.0}$) ranges from 240 to 310 K and there

256 is little difference in the PDFs of the 1B01-2A25-PMD and 1B01-2A25-GD. The PDF of $TB_{3.7}$ has a

257 multi-peak structure, whereas the PDFs of $TB_{10.8}$ and $TB_{12.0}$ are both single peaks (Fig. 3d–3f). Gridding

258 therefore does not result in dramatic variations of the parameters in the 1B01-2A25-PMD.

259 Statistical calculations were carried out to quantify the influence of gridding on the 1B01-2A25-PMD.

260 Table 2 shows the mean, standard deviation (STD) and the corresponding differences of the near-surface

261 rain rate and the signals from the five channels in the 1B01-2A25-PMD and 1B01-2A25-GD for orbit

262 37362 on 5 June 2004.

263 **Table2. Comparisons of statistical mean and standard deviation (STD) of the near-surface rain rate and**

264 **signals from five channels in the 1B01-2A25-PMD and 1B01-2A25-GD for orbit number 37362 on 5 June 2004.**

	Before gridding		After gridding		Difference	
	Mean	STD	Mean	STD	Mean	STD
RF1	0.112	0.195	0.110	0.189	0.002	0.006
RF2	0.083	0.126	0.082	0.123	0.001	0.003
$TB_{3.7}$	288.805	11.928	288.682	10.631	0.123	1.297
$TB_{10.8}$	280.516	16.120	280.521	15.397	-0.005	0.723
$TB_{12.0}$	278.584	16.574	278.628	15.882	-0.044	0.692
Near-surface rain rate	3.072	5.121	2.209	2.745	0.861	2.376

265 These results show that the difference in the mean value in this orbit is no more than 0.87 and the STD

266 is no more than 2.38. The differences in the near-surface rain rate are always larger than the differences

267   in the signals for the five channels, although all the differences are acceptable. The statistical results

268   quantitively verifiy that the slight influence caused by gridding can be neglected and the parameters in

269   the 1B01-2A25-GD are reliable.

270   **3.3   Presentation of the M-1B01-2A25-GD parameters**

271   The ERA5 atmospheric parameters are merged with the 1B01-2A25-GD to establish a new gridded

272   dataset (M-1B01-2A25-GD). The merging process among the 1B01, 2A25 and ERA5 datasets is based

273   on the 2A25, so the detection field is about the same as that measured by the TRMM PR in the new

274   merged dataset. Taking orbit 37362 on 5 June 2004 in the M-1B01-2A25-GD as an example.

275
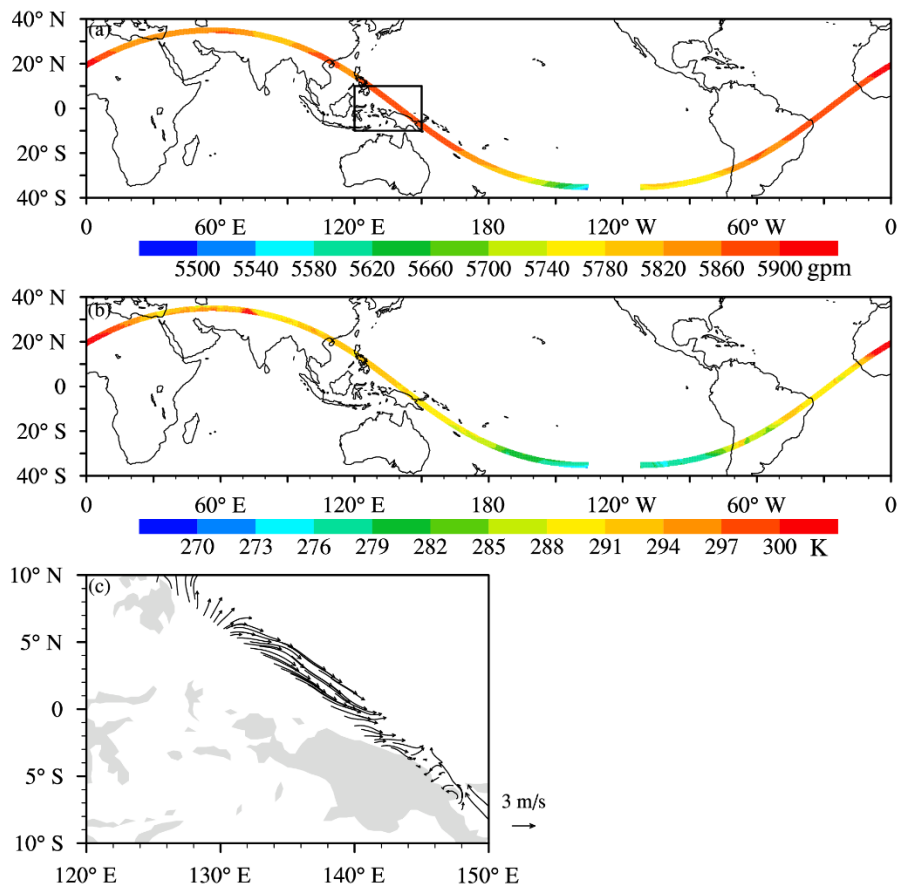
276   **Figure 4: Distribution of (a) the geopotential height at 500 hPa, (b) the temperature at 850 hPa and (c) the**

277   **wind field at 1000 hPa in orbit number 37362 on 5 June 2004 in the M-1B01-2A25-GD.**

278   Figure 4 shows the geopotential height at 500 hPa, the temperature at 850 hPa and the wind field at 1000

279   hPa. The geopotential height is mainly in the range 5540–5900 gpm and the temperature ranges from

280   270 to 300 K (Fig. 4a, 4b). The box in Fig. 4a shows an enlarged view of the wind field. A strong

281   northwesterly wind appears on the sea surface. The parameters for precipitation, clouds and the

282 atmospheric status provided by the M-1B01-2A25-GD can therefore be used to study the properties of

283 precipitation and clouds systems.

284 **3.4   Applications of the M-1B01-2A25-GD**

285 Evaluations of the M-1B01-2A25-GD show that the merging process does not seriously distort the

286 original data. The new dataset can therefore be used to analyze different types of precipitation and clouds

287 systems. To illustrate the applicability of this new dataset to a variety of different scenarios, we selected

288 precipitation on the trumpet-shaped topography of the Tibetan Plateau, typhoon Rananim precipitation

289 and frontal precipitation in eastern China for further analysis.

290 **3.4.1 Precipitation on the trumpet-shaped topography of the southern Tibetan Plateau**

291 The trumpet-shaped topography of the southern Tibetan Plateau (90°–100° E, 22°–32° N) is the one of

292 the main channel for the transport of water vapor in this region. The topography here is complex and

293 there is a clear difference in altitude in the trumpet-shaped area from the hills below the Tibetan

294 Plateau to the steep slopes and the central Tibetan Plateau. Define these three types of topography as

295 the foreland under the Tibetan Plateau (FTP), the slope of the trumpet-shaped area (STS) and the

296 central part of the Tibetan Plateau (CTP).

297
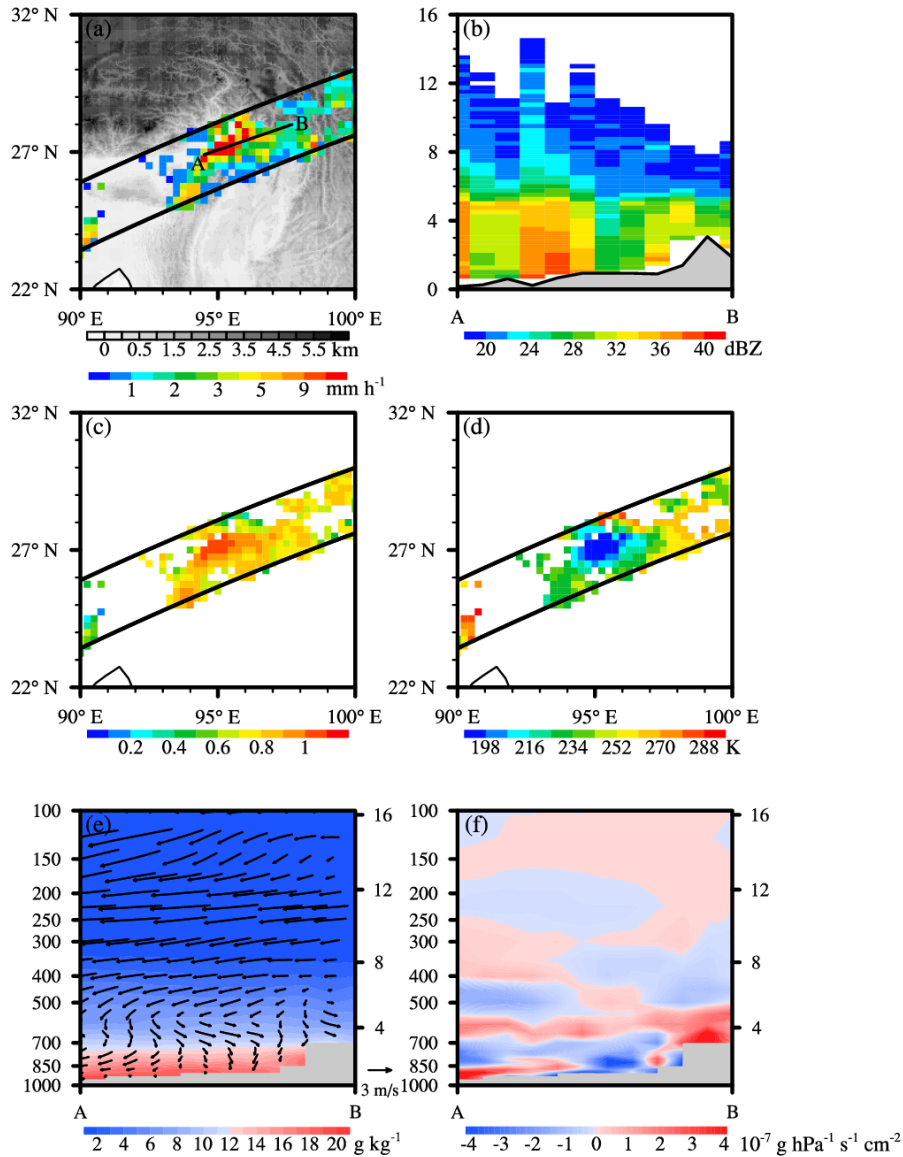
Figure 5: Case study of precipitation in the trumpet-shaped topography on the Tibetan Plateau on 2 July 2004
(orbit number 37786). (a) The near-surface rain rate, (b) vertical cross-sections of the precipitation reflectivity
factor, (c) RF1, (d) TB$_{10.8}$, vertical cross-sections of (e) the wind vectors and specific humidity and (f) the
divergence of water vapor flux along line A-B in panel (a).

The precipitation occurred on 2 July 2004 (orbit number 37786). Intense rainfall mainly occurs on the

STS with a maximum precipitation intensity over 13 mm h^{-1}. Fig. 5a shows the near-surface rain rate in

the rain belt and Fig. 5b shows the vertical cross-section of the precipitation reflectivity factor in the

direction of the heavy rainfall center shown in Fig. 5a (line A–B). The altitude varies by 2 km from A to

B. The storm top height (STH) refers to the height at which the precipitation reflectivity factor of the

three continuous layers is greater than 16 dBZ in the precipitation profiles, decreases gradually and the

strong reflectivity factor weakens over the CTP. The intensity of precipitation on the STS from the

309   atmosphere to the land surface first increases and then decreases. There is usually a strong precipitation

310   reflectivity factor 3 km above the land surface. However, the intensity of precipitation on CTP is weaker

311   than that in the FTP. Fu et al. (2017) showed that the elevation of water vapor by the complex topography

312   leads to precipitation on the STS. However, the intensity of precipitation is weak because the water vapor

313   column on the CTP is inadequate due to earlier precipitation on the STS.

314   The physical characteristics of the precipitating clouds are different as a result of the differences in the

315   intensity of precipitation. Fig. 5c shows RF1, which ranges between 0.5 and 1.0, with high values in the

316   areas where precipitation is heavy. $TB_{10.8}$ varies from 190 to 210 K in the region of intense precipitation,

317   which shows that the cloud-top is high. The cloud-top is slightly lower around the precipitating cloud

318   where $TB_{10.8}$ is high (Fig. 5d). In addition to the topographic elevation of water vapor, it is also necessary

319   to understand the status of the atmosphere, including the wind field and water vapor conditions.

320   There is a wet band below 700 hPa with a specific humidity over 15 g kg^{-1}. The specific humidity

321   decreases in the lower layers of the atmosphere from the FTP to the STS and extending to the CTP. A

322   northeasterly airflow prevails below 700 hPa from the CTP via the STS to the FTP. Between 700 and

323   500 hPa, this northeasterly airflow turns to the northwest over the CTP. Above 500 hPa, the airflow is

324   mainly westerly with a higher speed. The water vapor content becomes less favorable for precipitation

325   in the higher atmospheric layers (Fig. 5e). The better water vapor conditions in the lower atmosphere are

326   important for the precipitation process. The upward airflow toward the CTP brings abundant water vapor

327   from the FTP via the STS to the CTP.

328   The water vapor flux divergence (WVFD) is an important parameter used to describe the status of water

329   vapor transportation in the atmosphere. The WVFD of the FTP is about $1\text{-}3\times10^{-7}$ g hPa^{-1} s^{-1} cm^{-2}, which

330   means that the water vapor is diverging. The divergence belt extends to the front of the STS. The WVFD

331   changes to positive on the STS (from -2×10^{-7} to 0 g hPa^{-1} s^{-1} cm^{-2}), so the water vapor here is in a

332   convergence field. There is strong divergence on the CTP with a maximum more than 4×10^{-7} g hPa^{-1} s^{-1}

333   cm^{-2}. Fig. 5f shows the complex water vapor transportation processes from the FTP to the CTP. Most of

334   the transport and exchange of water vapor occurs in the lower atmosphere. There is more water vapor in

335   the FTP and STS than in the CTP and the intensity of precipitation is heavy in the STS. The elevated

336   topography increases the transportation of water vapor and chance of precipitation, the wind speed and

337   convergence of water vapor indeed favor heavy rainfall over the STS.

338 **3.4.2 Typhoon Rananim precipitation**

339 Second precipitation example, Typhoon Rananim, occurred in the western Pacific (16°–26° N, 122°–132°

340 E) at orbit 38395 on 10 August 2004.
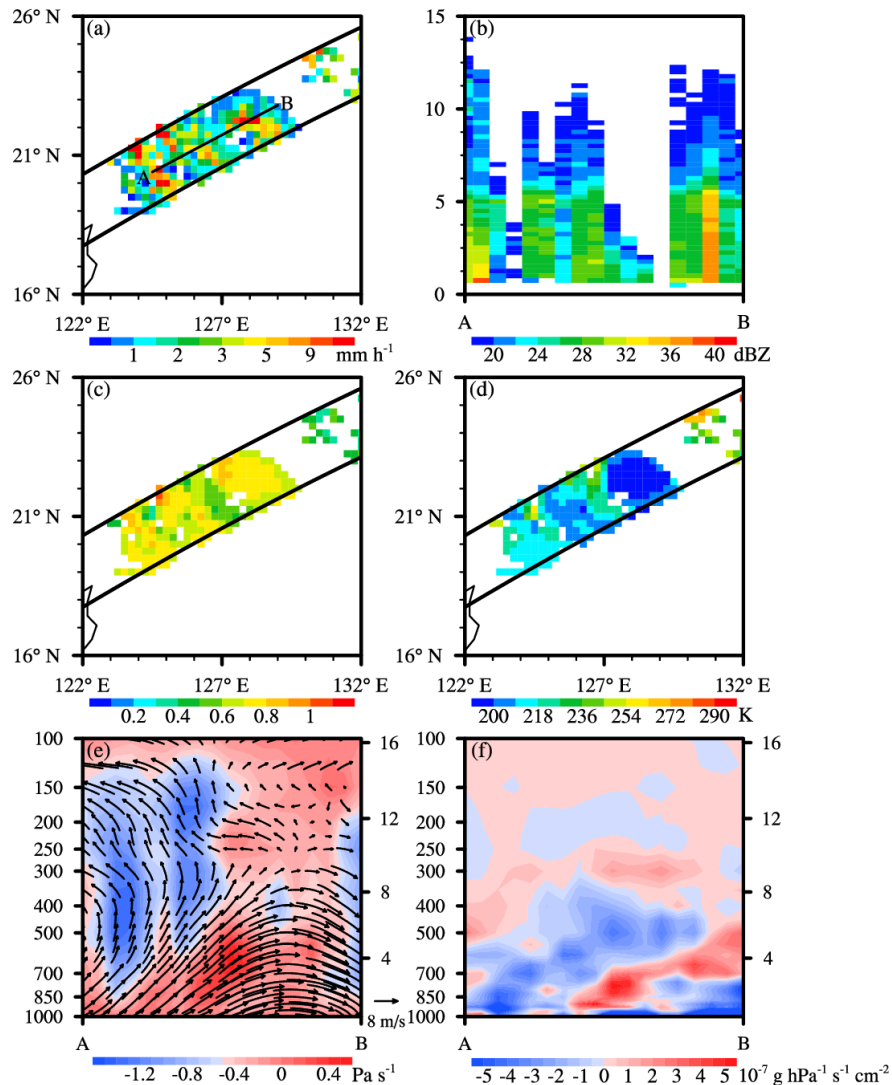
341

342 **Figure 6: Case study of Typhoon Rananim precipitation on 10 August 2004 (orbit number 38395). (a) The**

343 **near-surface rain rate, (b)vertical cross-sections of the precipitation reflectivity factor, (c) RF1, (d) TB$_{10.8}$,**

344 **vertical cross-sections of (e) the wind vectors and vertical velocity and (f) the divergence of water vapor flux**

345 **along line A-B in panel (a).**

346 The eye of a typhoon is an important indicator over the whole lifetime of the typhoon. The eye of the

347 typhoon shown in Fig. 6a means the typhoon is on the mature stage and the cross-section along line A–

348 B crosses the middle of the eye. The STH is higher than 13 km in the eye wall region, which means that

349 strong convection occurs here, but is lower than 5 km in the eye of the typhoon. The maximum

350 precipitation reflectivity factor exceeds 35 dBZ, but the precipitation intensity inside the eye is weak,

351   resulting in a low precipitation reflectivity factor and STH (Fig. 6b).

352   RF1 varies from 0.5 to 1. The value near the precipitating cloud-top are small near the eye wall (Fig. 6c).

353   The distribution of $TB_{10.8}$ shows the height of the precipitating cloud-top, which also indirectly represents

354   convection inside the precipitation system. $TB_{10.8}$ is less than 235 K around the eye of the typhoon. A

355   low brightness temperature means a high precipitating cloud-top. The STH is low and the cloud-top is

356   high in some regions as a result of cirrus clouds (Fig. 6d). The maximum descending speed in the typhoon

357   eye is over 0.5 Pa s^{-1} and a southwesterly airflow prevails at high speeds below 400 hPa. The airflow is

358   in the opposite direction at low speeds above 400 hPa. The maximum ascending speed in the eye wall

359   reaches -1.5 Pa s^{-1} (Fig. 6e).

360   Figure 6f shows the transportation of water vapor in the typhoon system along line A–B. There is strong

361   convergence of water vapor below 700 hPa and the maximum WVFD is -5×10^{-7}g hPa^{-1} s^{-1} cm^{-2}. There

362   exists a belt of divergence in the middle of the convergence field with WVFD values ranging from 2×10^{-7}

363   to 5×10^{-7} g hPa^{-1} s^{-1} cm^{-2}. Water vapor is usually transported in the lower layers of the atmosphere.

364   Water vapor is exchanged between the typhoon and the eye wall, so the intensity of precipitation is

365   different at various locations in the typhoon system.

366   **3.4.2 Frontal precipitation in eastern China**

367   In frontal systems, precipitation is induced by the elevation of air masses when two types of air flow

368   meet. As an example, frontal precipitation case that occurred in eastern China (30°–40° N, 112°–122° E)

369   on 22 June 2003 at orbit 31926 is analyzed.

370
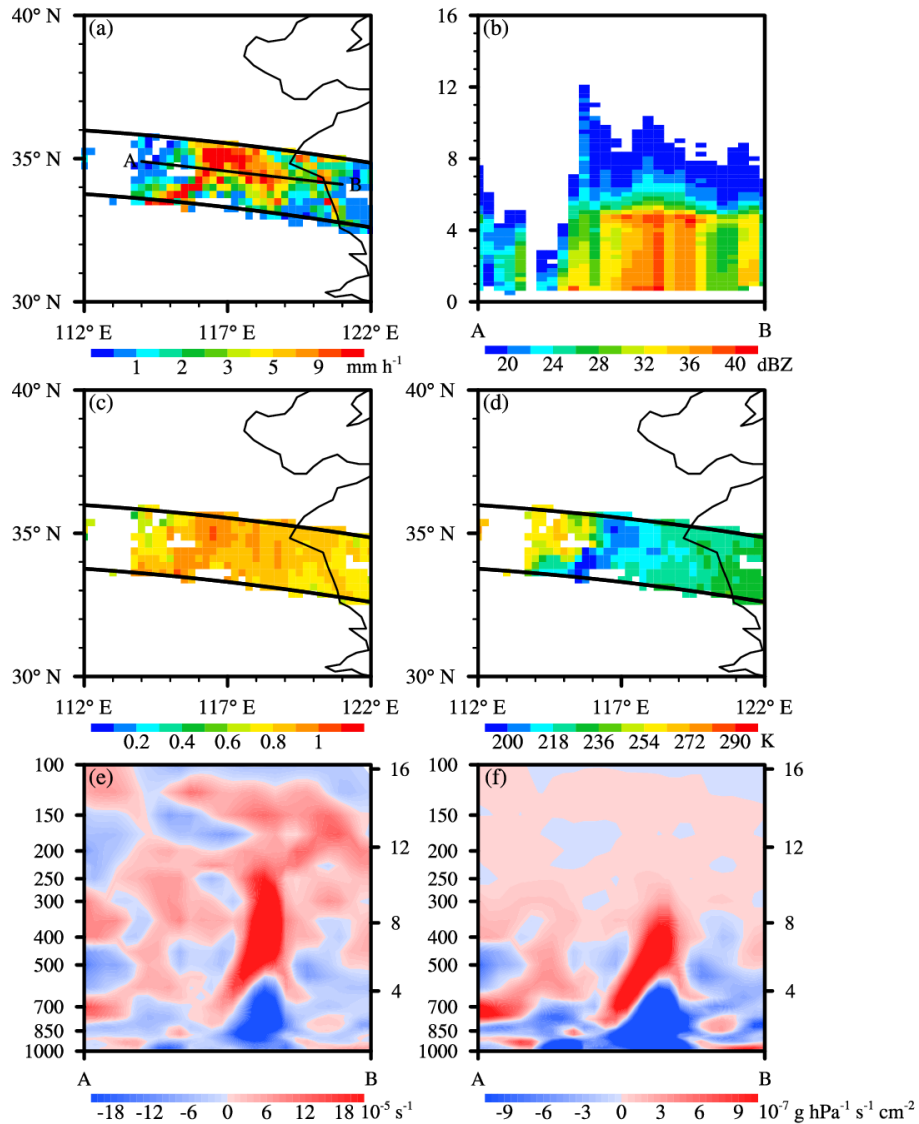
Figure 7: Case study of frontal precipitation on 3 June 2003 (orbit number 31926). (a) The near-surface rain rate, vertical cross-sections of (b) the precipitation reflectivity factor, (c) RF1, (d) TB$_{10.8}$, vertical cross-sections of (e) divergence and (f) the divergence of water vapor flux along line A-B in panel (a).

Fig. 7a clearly shows the rain belt at the boundary of the different airflows. The maximum precipitation intensity is more than 10 mm h^{-1}. Fig. 7b shows the precipitation reflectivity factor profiles of line A–B to illustrate the vertical structure. The reflectivity factor is high from the land surface to 5 km and the maximum exceeds 42 dBZ. The RF1 shows a high value which is bigger than 0.8 near the heavy rainfall region (Fig. 7c). TB$_{10.8}$ varies between 200 and 235 K in the area of strong precipitation intensity and the minimum appears in the front, where the height of the precipitating cloud-top is highest. The difference in the brightness temperature on each side of the front represents the difference in the height of the precipitating cloud-top (Fig. 7d). Figure 7e shows that the calculated divergence in the cross-section,

382   which represents convergence below 700 hPa, reaches -18×10^{-5} s^{-1}. Strong divergence over 18×10^{-5} s^{-1}

383   occurs above 500 hPa. The WVFD has the same distribution as the divergence. The maximum WVFD

384   exceeds -10×10^{-7} g hPa^{-1} s^{-1} cm^{-2} below 700 hPa. Strong divergence of the water vapor occurs above

385   500 hPa, with a WVDF of 9×10^{-7}g hPa^{-1} s^{-1} cm^{-2}. The exchange of water vapor often occurs below 200

386   hPa (Fig. 6f). The atmospheric status satisfies the precipitation condition and shows the complexity of

387   vertical motion in the atmosphere.

388 **4   Discussion**

389   Due to the rapid development of the technology of satellite and emergence of the various satellite data

390   products. Huge amount of the satellite datasets usually leads to difficulty in data storage. The M-1B01-

391   2A25-GD is a grid-level dataset with spatial resolution of 0.25° which can largely reduce the digital

392   storage space required. This new dataset will become a demonstration for satellite data processing.

393   The data merging among the precipitation parameters (profiles of rain rate and precipitation reflectivity

394   factor, near-surface rain rate and rain type) measured by the PR, spectral signals measured by the VIRS

395   and atmospheric parameters (temperature, specific humidity, wind field, geopotential height, divergence

396   and vertical velocity) of the ERA5 reanalysis dataset is an initial attempt. This dataset can be helpful in

397   studying the characteristics and changes in precipitation and the clouds systems. To further explore the

398   relationship among the precipitation, clouds and atmospheric parameters, the cloud parameters based on

399   the signals retrival from the TRMM VIRS data will be added to the merged dataset. The work is now in

400   progress and will not be involved in this study due to the limited length of the paper.

401   The studies on the atmospheric dynamics and cloud physics are isolated because of the lack of the suitable

402   datasets. Now, the problem can be solved through establishing the new merged dataset. The

403   comprehensive parameters about precipitation, clouds and atmosphere status can be obtained in each

404   single orbit from the M-1B01-2A25-GD to support the case analysis and model simulations.

405 **5   Data availability**

406   The used M-1B01-2A25-GD in this paper are accessible at http://doi.org/10.5281/zenodo.4458868 (Sun

407   and Fu, 2021).

6   Conclusions

We establish a new merged gridded dataset M-1B01-2A25-GD combining satellite and reanalysis datasets. The precipitation, cloud and atmospheric parameters are spatially and temporally collocated. The gridded data helps to reduce the digital storage space required. The statistical results show that there is no obvious bias in the 1B01-2A25-PMD when compared with the original swath-level data measured by the TRMM VIRS. The 1B01-2A25-GD has the same spatial resolution as the ERA5 reanalysis dataset. The average inside the grid leads to smoothing effects on the maximum and minimum values, but does not adversely influence the parameters in the 1B01-2A25-PMD. In the arbitrarily choosen orbit, the difference in the mean value is no more than 0.87 and the STD is no more than 2.38 for the near-surface rain rate and signals measured by the VIRS. The M-1B01-2A25-GD contains comprehensive parameters about precipitation, clouds and the atmosphere that are useful in studies of the characteristics and distribution of precipitation and clouds systems in the tropics and subtropics. Three typical applications of the M-1B01-2A25-GD are introduced by analyzing different examples of precipitation. This new dataset can support studies of precipitation, clouds systems and model simulations. Longer time periods of data and more parameters will be added as satellite technology and models are improved.

Author contribution. Lilu Sun and Yunfei Fu prepared the data in the standardized format. Lilu Sun uploaded the data in the data repository and prepared the manuscript with contributions from all co-authors.

Competing interests. The authors declare that they have no conflict of interests.

Financial   support.   This   research   was   supported   by   the National Natural Science Foundation of China (Grants 91837310, 41675041).

References

Awaka, J., Iguchi, T., Kumagai, H., and Okamoto, K.: Rain type classification algorithm for TRMM precipitation radar, IEEE International Geoscience and Remote Sensing Symposium Proceedings. Remote Sensing - A Scientific Vision for Sustainable Development, Singapore, 3-8 August 1997,

https://doi.org/10.1109/IGARSS.1997.608993, 1997.

Baker, M. B.: Cloud Microphysics and Climate, Science, 276, 1072-1078, https://doi.org/10.1126/science.276.5315.1072, 1997.

Chen, F., and Fu, Y. F.: Characteristics of typhoon precipitation and non-typhoon precipitation over East Asia based on merged PR and VIRS data, Climatic. Environ. Res. (in Chinese), 20, 62-74, https://doi.org/10.3878/j.issn.1006-9585.2014.14031, 2015.

Chen, F., Sheng, S., Bao, Z., Wen, H., Hua, L., Paul, N. J., and Fu, Y.: Precipitation Clouds Delineation Scheme in Tropical Cyclones and Its Validation Using Precipitation and Cloud Parameter Datasets from TRMM, J. Appl. Meteorol. Climatol., 57, 821-836, https://doi.org/10.1175/jamc-d-17-0157.1, 2018.

Chen, Y., and Fu, Y.: Characteristics of VIRS Signals within Pixels of TRMM PR for Warm Rain in the Tropics and Subtropics, J. Appl. Meteorol. Climatol., 56, 789-801, https://doi.org/10.1175/jamc-d-16-0198.1, 2017.

Durden, S. L., Im, E., Haddad, Z. S., and Li, L.: Comparison of TRMM precipitation radar and airbrone radar data, J. Appl. Meteorol., 42, 769-774, https://doi.org/10.1175/1520-0450(2003)0422.0.CO;2, 2003.

Fu, Y. F. and Liu, G. S.: The variability of tropical precipitation profiles and its impact on microwave brightness temperatures as inferred from TRMM data, J. Appl. Meteorol., 40, 2130-2143, https://doi.org/10.1175/1520-0450(2001)0402.0.CO;2, 2001.

Fu, Y., Liu, G., Wu, G., Yu, R., Xu, Y., Wang, Y., Li, R., and Liu, Q.: Tower mast of precipitation over the central Tibetan Plateau summer, Geophys. Res. Lett., 33, https://doi.org/10.1029/2005gl024713, 2006.

Fu, Y., Liu, Q., Gao, Y., Hong, X., Zi, Y., Zheng, Y., Li, R., and Heng, Z.: A feasible method for merging the TRMM microwave imager and precipitation radar data, J. Quant. Spectrosc. Ra., 122, 155-169, https://doi.org/10.1016/j.jqsrt.2012.08.028, 2013.

Fu, Y., Pan, X., Xian, T., Liu, G., Zhong, L., Liu, Q., Li, R., Wang, Y., and Ma, M.: Precipitation characteristics over the steep slope of the Himalayas in rainy season observed by TRMM PR and VIRS, Clim. Dynam., 51, 1971-1989, https://doi.org/10.1007/s00382-017-3992-3, 2017.

Fu, Y., and Zhang, A.: Life Cycle Effects on the Vertical Structure of Precipitation in East China Measured by Himawari-8 and GPM DPR, Mon. Weather. Rev., 146, 2183-2199, https://doi.org/10.1175/mwr-d-18-0085.1, 2018.

462   Fu, Y. F., Liu, Q., Zi, Y., Feng, S., Li, Y., and Liu, G. S.: Summer Precipitation andLatent Heating over

463   the Tibet Plateau Based on TRMM Measurements, Plateau. Mountain. Meteor. Res. (in Chinese), 28, 8-

464   18, https://doi.org/10.3969/j.issn.1674-2184.2008.01.002, 2008.

465   Fu, Y. F., Liu, P., Liu, Q., Ma, M., Sun, L., and Wang, Y.: Climatological Characteristics of VIRS

466   Channels for Precipitating Cloud in Summer Over the Tropics and Subtropics, Journal of Atmospheric

467   and Environmental Optics (in Chinese), 6, 129-140, https://doi.org/10.3969/j.issn.1673-

468   6141.2011.02.009, 2011.

469   Fu, Y. F.: Cloud Parameyers retrieved by the bispectral reflectance algorithm and associated applications,

470   J. Meteorol. Res-Prc., 28, 965-982, https://doi.org/CNKI:SUN:QXXW.0.2014-05-019, 2014.

471   Gao, W., Liu, L., Li, J., and Lu, C.: The Microphysical Properties of Convective Precipitation Over the

472   Tibetan Plateau by a Subkilometer Resolution Cloud-Resolving Simulation, J. Geophys. Res-Atmos.,

473   123, 3212-3227, https://doi.org/10.1002/2017jd027812, 2018.

474   Hartmann, D. L., and Short, D. A.: On the Use of Earth Radiation Budget Statistics for Studies of Clouds

475   and Climate, J. Atmos. Sci., 37, 1233-1250, https://doi.org/10.1175/1520-

476   0469(1980)037<1233:Otuoer>2.0.Co;2, 1980.

477   Hawkins, J., Miller, S., Mitrescu, C., L'Ecuyer, T., Turk, J., Partain, P., and Stephens, G.: Near-Real-Time

478   Applications of CloudSat Data, J. Appl. Meteorol. Climatol., 47, 1982-1994,

479   https://doi.org/10.1175/2007jamc1794.1, 2008.

480   Hayasaka, T., Kozu, T., Iguchi, T., Meneghini, R., Awaka, J., Okamoto, K. i., Wu, D. L., Jin, Y., and Jiang,

481   J.: Preliminary test results of a rain rate profiling algorithm for the TRMM precipitation radar, Microwave

482   Remote Sensing of the Atmosphere and Environment, China, 19 August 1998,

483   https://doi.org/10.1117/12.319497, 1998.

484   Heng, Z., and Fu, Y. F.: Impact of gridding scale on TRMM microwave imager cloud water information,

485   Climatic. Environ. Res. (in Chinese), 19, 693-702, https://doi.org/10.3878/j.issn.1006-9585.2013.13049,

486   2014.

487   Hersbach, H., Bell, B., Berrisford, P., Hirahara, S., Horányi, A., Muñoz-Sabater, J., Nicolas, J., Peubey,

488   C., Radu, R., Schepers, D., Simmons, A., Soci, C., Abdalla, S., Abellan, X., Balsamo, G., Bechtold, P.,

489   Biavati, G., Bidlot, J., Bonavita, M., Chiara, G., Dahlgren, P., Dee, D., Diamantakis, M., Dragani, R.,

490   Flemming, J., Forbes, R., Fuentes, M., Geer, A., Haimberger, L., Healy, S., Hogan, R. J., Hólm, E.,

491   Janisková, M., Keeley, S., Laloyaux, P., Lopez, P., Lupu, C., Radnoti, G., Rosnay, P., Rozum, I., Vamborg,

492   F., Villaume, S., and Thépaut, J. N.: The ERA5 global reanalysis, Q. J. R. Meteorol. Soc., 146, 1999-

493   2049, https://doi.org/10.1002/qj.3803, 2020.

494   Hobbs, P. V.: Research on the clouds and precipitation past present and future,Part II, Bull. Am. Meteorol.

495   Soc., 72, 184-191, https://doi.org/10.1175/1520-0477(1991)072<0184:ROCAPP>2.0.CO;2, 1991.

496   Houze, R. A.: Structures of atmospheric precipitation systems A global survey, Radio. Sci., 16, 671-689,

497   https://doi.org/10.1029/RS016i005p00671, 1981.

498   Houze, R. A.: Stratiform Precipitation in Regions of Convection: A Meteorological Paradox?, Bull. Am.

499   Meteorol. Soc., 78, 2179-2196, https://doi.org/10.1175/1520-0477(1997)078<2179:SPIROC>2.0.CO;2,

500   1997.

501   Iguchi, T., Meneghini, R., Awaka, J., Kozu, T., and Okamoto, K.: Rain profiling algorithm for TRMM

502   Precipitation Radar data, Adv. Space. Res., 25, 973-976, https://doi.org/10.1016/S0273-1177(99)00933-

503   3, 2000.

504   Kienast-Sjögren, E., Rolf, C., Seifert, P., Krieger, U. K., Luo, B. P., Krämer, M., and Peter, T.:

505   Climatological and radiative properties of midlatitude cirrus clouds derived by automatic evaluation of

506   lidar measurements, Atmos. Chem. Phys., 16, 7605-7621, https://doi.org/10.5194/acp-16-7605-2016,

507   2016.

508   Kozu, T., Kawanishi, T., Kuroiwa, H., Oikawa, M., Kumagai, H., Okamoto, K., Okumura, M., Nakatsuka,

509   H., and Nishikawa, K.: Development of precipitation radar onboard the Tropical Rainfall Measuring

510   Mission   (TRMM)   satellite.,   IEEE.   Trans.   Geosci.   Remote.   Sens.,   39,   102-116,

511   https://doi.org/10.1109/36.898669, 2001.

512   Kummerow, C., William, S., and Giglio, L.: A simplified scheme for obtaining precipitation and vertical

513   hydrometeor profiles from passive microwave sensors, IEEE. Trans. Geosci. Remote. Sens., 34, 1213-

514   1232, https://doi.org/10.1109/36.536538, 1996.

515   Kummerow, C., Barnes, W., Kozu, T., Shiue, J., and Simpson, J.: The tropical rainfall measuring mission

516   (TRMM) sensor package, J. Atmos. Ocean. Tech., 15, 809-817, https://doi.org/10.1175/1520-

517   0426(1998)015<0809:TTRMMT>2.0.CO;2, 1998.

518   Kummerow, C., Simpson, J., Thiele, O., Barnes, W., Chang, A. T. C., Stocker, E., Adler, R. F., Hou, A.,

519   Kakar, R., Wentz, F., Ashcroft, P., Kozu, T., Hong, Y., Okamoto, K., Iguchi, T., Kuroiwa, H., Im, E.,

Haddad, Z., Huffman, G., Ferrier, B., Olson, W. S., Zipser, E., Smith, E. A., Wilheit, T. T., North, G., Krishnamurti, T., and Nakamura, K.: The status of the TRMM after two years in orbit, J. Appl. Meteorol. Climatol., 39, 1965-1982, https://doi.org/10.1175/1520-0450(2001)040<1965:TSOTTR>2.0.CO;2, 2000.

Lau, K. M., and Wu, H. T.: Characteristics of Precipitation, Cloud, and Latent Heating Associated with the Madden-Julian Oscillation, J. Climate., 23, 504-518, https://doi.org/10.1175/2009jcli2920.1, 2010.

Li, J., Lv, Q., Jian, B., Zhang, M., Zhao, C., Fu, Q., Kawamoto, K., and Zhang, H.: The impact of atmospheric stability and wind shear on vertical cloud overlap over the Tibetan Plateau, Atmos. Chem. Phys., 18, 7329-7343, https://doi.org/10.5194/acp-18-7329-2018, 2018.

Li, R., and Fu, Y. F.: Tropical Precipitation Estimated by GPCP and TRMM PR Observations, Adv. Atmos. Sci., 22, 852-864, https://doi.org/10.1007/BF02918685, 2005.

Liou, K.-N.: Influence of Cirrus Clouds on Weather and Climate Processes: A Global Perspective, Mon. Weather. Rev., 114, 1167-1199, https://doi.org/10.1175/1520-0493(1986)114<1167:Ioccow>2.0.Co;2, 1986.

Liu, C., and Zipser, E. J.: "Warm Rain" in the Tropics: Seasonal and Regional Distributions Based on 9 yr of TRMM Data, J. Climate., 22, 767-779, https://doi.org/10.1175/2008jcli2641.1, 2009.

Liu, G. S., and Fu, Y. F.: The Characteristics of tropical precipitation profiles as inferred from satellite radar measurements, J. Meteorol. Soc. Jpn., 79, 131-143, https://doi.org/10.2151/jmsj.79.131, 2001.

Liu, Q., and Fu, Y. F.: Characteristics of latent heating over the Tibetan Plateau during summer, Journal of University of Science and Technology of China (in Chinese), 37, 303-309, https://doi.org/10.3969/j.issn.0253-2778.2007.03.015, 2007.

Liu, Q., and Fu, Y.: Comparison of radiative signals between precipitating and non-precipitating clouds in frontal and typhoon domains over East Asia, Atmos. Res., 96, 436-446, https://doi.org/10.1016/j.atmosres.2010.02.003, 2010.

Lu, D., Yang, Y., and Fu, Y.: Interannual variability of summer monsoon convective and stratiform precipitations in East Asia during 1998-2013, Int. J. Climatol., 36, 3507-3520, https://doi.org/10.1002/joc.4572, 2016.

Luo, S., Fu, Y., Zhou, S., Wang, X., and Wang, D.: Analysis of the Relationship between the Cloud Water Path and Precipitation Intensity of Mature Typhoons in the Northwest Pacific Ocean, Adv. Atmos. Sci.,

37, 359-376, https://doi.org/10.1007/s00376-020-9204-9, 2020.

Luo, Y., Zhang, R., and Wang, H.: Comparing Occurrences and Vertical Structures of Hydrometeors between Eastern China and the Indian Monsoon Region Using CloudSat/CALIPSO Data, J. Climate., 22, 1052-1064, https://doi.org/10.1175/2008jcli2606.1, 2009.

Min, Q., Li, R., Wu, X., and Fu, Y.: Retrieving latent heating vertical structure from cloud and precipitation Profiles—Part I: Warm rain processes, J. Quant. Spectrosc. Ra., 122, 31-46, https://doi.org/10.1016/j.jqsrt.2012.11.030, 2013.

Nesbitt, S. W., Zipser, E. J., and Cecil, D. J.: A census of precipitation features in the tropics using TRMM Radar, ice scattering, and lightning observations, J. Climate., 13, 4087-4106, https://doi.org/10.1175/1520-0442(2000)0132.0.CO;2, 1999.

Oki, T., and Kanae, S.: Global hydrological cycles and world water resources, Science, 313, 1068-1072, https://doi.org/10.1126/science.1128845, 2006.

Olson, W. S., Kummerow, C. D., Heymsfield, G. M., and Giglio, L.: A Method for Combined Passive-Active Microwave Retrievals of Cloud and Precipitation Profiles, J. Appl. Meteorol., 35, 1763-1789, https://doi.org/10.1175/1520-0450(1996)035<1763:Amfcpm>2.0.Co;2, 1996.

Pan, X., and Fu, Y. F.: Analysis on Climatological Characteristics of Deep and Shallow Precipitation Cloud in Summer over Qinghai-Xizang Plateau, Plateau. Meteor. (in Chinese), 34, 1191-1203, https://doi.org/10.7522/j.issn.1000-0534.2014.00112, 2015.

Petty, G. W.: Physical retrievals of over-ocean rain rate from multichannel microwave imagery. Part I: Theoretical Characteristics of Normalized Polarization and Scattering Indices, Meteorol. Atmos. Phys., 54, 79-99, https://doi.org/10.1007/BF01030054, 1994.

Roscow, William, B., and Robert, A.: Advances in understanding clouds from ISCCP, Bull. Am. Meteorol. Soc., 80, 2261-2288, https://doi.org/10.1175/1520-0477(1999)080<2261:AIUCFI>2.0.CO;2, 1999.

Sassen, K., Wang, Z., and Liu, D.: Cirrus clouds and deep convection in the tropics: Insights from CALIPSO and CloudSat, J. Geophys. Res., 114, D00H06, https://doi.org/10.1029/2009jd011916, 2009.

Schumacher, C., and Houze, R. A.: The TRMM precipitation radar's view of shallow, isolated rain, J. Appl. Meteorol., 42, 1519-1524, https://doi.org/10.1175/1520-0450(2003)042<1519:TTPRVO>2.0.CO;2, 2003.

Simpson, J., Kummerow, C., Tao, W.-K., and Adler, R. F.: On the Tropical Rainfall Measuring Mission

578 (TRMM), Meteorol. Atmos. Phys., 60, 19-36, https://doi.org/10.1007/BF01029783, 1996.

579 Sun, L. L., and Fu, Y. F.: A new merged dataset for analyzing clouds, precipitation and atmospheric

580 parameters based on ERA5 reanalysis data and the measurements of TRMM PR and VIRS. Zenodo,

581 http://doi.org/10.5281/zenodo.4458868, 2021.

582 Szoke, E. J., Zipser, E. J., and Jorgensen, D. P.: A Radar Study of Convective Cells in Mesoscale Systems

583 in GATE. Part I: Vertical Profile Statistics and Comparison with Hurricanes, J. Atmos. Sci., 43, 182-198,

584 https://doi.org/10.1175/1520-0469(1986)043<0182:Arsocc>2.0.Co;2, 1986.

585 Tustison, B., Foufoula-Georgiou, E., and Harris, D.: Scale-recursive estimation for multisensor

586 Quantitative Precipitation Forecast verification: A preliminary assessment, J. Geophys. Res., 108, CIP2-

587 1-14 https://doi.org/10.1029/2001jd001073, 2002.

588 Wang, R., and Fu, Y.: Structural characteristics of atmospheric temperature and humidity inside clouds

589 of convective and stratiform precipitation in the rainy season over East Asia, J. Meteorol. Res-Prc., 31,

590 890-905, https://doi.org/10.1007/s13351-017-7038-x, 2017.

591 Wang, R., Fu, Y., Xian, T., Chen, F., Yuan, R., Li, R., and Liu, G.: Evaluation of Atmospheric Precipitable

592 Water Characteristics and Trends in Mainland China from 1995 to 2012, J. Climate., 30, 8673-8688,

593 https://doi.org/10.1175/jcli-d-16-0433.1, 2017.

594 Wang, Y., Zhang, Y., Fu, Y., Li, R., and Yang, Y.: A climatological comparison of column-integrated water

595 vapor for the third-generation reanalysis datasets, Sci. China Earth Sci., 59, 296-306,

596 https://doi.org/10.1007/s11430-015-5183-6, 2015.

597 Wetherald, R. T., and Manabe, S.: Cloud Feedback Processes in a General Circulation Model, J. Atmos.

598 Sci., 45, 1397-1416, https://doi.org/10.1175/1520-0469(1988)045<1397:Cfpiag>2.0.Co;2, 1988.

599 Wilheit, T. T., Chang, A. T. C., V. Rao, M. S., Rodgers, E. B., and Theon, J. S.: A Satellite Technique for

600 Quantitatively Mapping Rainfall Rates over the Oceans, J. Appl. Meteorol., 16, 551-560,

601 https://doi.org/10.1175/1520-0450(1977)016<0551:Astfqm>2.0.Co;2, 1977.

602 Xia, J., and Fu, Y. F.: The vertical characteristics of temperature and humidity inside convective and

603 stratiform precipitating clouds in the East Asian summer monsoon region and Indian summer monsoon

604 region, Chinese. J. Atmos. Sci. (in Chinese), 40, 563-580, https://doi.org/10.3878/j.issn.1006-

605 9895.1507.15123, 2016.

606 Yang, Y.-J., Lu, D.-R., Fu, Y.-F., Chen, F.-J., and Wang, Y.: Spectral Characteristics of Tropical Anvils

Obtained by Combining TRMM Precipitation Radar with Visible and Infrared Scanner Data, Pure Appl. Geophys., 172, 1717-1733, https://doi.org/10.1007/s00024-014-0965-x, 2014.

Yuter, S. E., and Houze, R. A.: Three-Dimensional Kinematic and Microphysical Evolution of Florida Cumulonimbus. Part III: Vertical Mass Transport, Mass Divergence, and Synthesis, Mon. Weather. Rev., 123, 1964-1983, https://doi.org/10.1175/1520-0493(1995)123<1964:TDKAME>2.0.CO;2, 1995.

Zhao, B., Zhang, B., Shi, C., Liu, J., and Jiang, L.: Comparison of the Global Energy Cycle between Chinese Reanalysis Interim and ECMWF Reanalysis, J. Meteorol. Res-Prc., 33, 563-575, https://doi.org/10.1007/s13351-019-8129-7, 2019.

Zheng, X. Y., Fu, Y. F., Yang, Y. J., and Liu, G. S.: Impact of atmospheric circulations on aerosol distributions in autumn over eastern China: observational evidence, Atmos. Chem. Phys., 15, 12115-12138, https://doi.org/10.5194/acp-15-12115-2015, 2015.

Zipser, E. J., and Lutz, K. R.: The Vertical Profile of Radar Reflectivity of Convective Cells: A Strong Indicator of Storm Intensity and Lightning Probability?, Mon. Weather. Rev., 122, 1751-1759, https://doi.org/10.1175/1520-0493(1994)122<1751:Tvporr>2.0.Co;2, 1994.